MRS Communications (2020), 1 of 7

doi:10.1557/mrc.2019.166

MRS Communications

Research Letter

Deep learning-based super-resolution for small-angle neutron scattering data: attempt to accelerate experimental workflow

Ming-Ching Chang and **Yi Wei,** University at Albany, State University of New York, New York, NY, USA
Wei-Ren Chen and **Changwoo Do**, Neutron Scattering Division, Oak Ridge National Laboratory, Oak Ridge, TN, USA
Address all correspondence to Changwoo Do at **doc1@ornl.gov**

(Received 15 November 2019; accepted 19 December 2019)

Abstract

The authors propose an alternative route to circumvent the limitation of neutron flux using the recent deep learning super-resolution technique. The feasibility of accelerating data collection has been demonstrated by using small-angle neutron scattering (SANS) data collected from the EQ-SANS instrument at Spallation Neutron Source (SNS). Data collection time can be reduced by increasing the size of binning of the detector pixels at the sacrifice of resolution. High-resolution scattering data is then reconstructed by using a deep learning-based super-resolution method. This will allow users to make critical decisions at a much earlier stage of data collection, which can accelerate the overall experimental workflow.

Introduction

It is now a common practice of using neutron scattering techniques to investigate atomic-scale structure and dynamics. They possess unique advantages over other scattering techniques, such as x-ray or light, with the exceptional penetration power, free from radiation damage, and the ability to selectively highlight specific parts of materials via isotope labeling.[1,2] However, the currently available neutron flux is significantly lower than that of photons generated by modern synchrotron radiation or free-electron laser sources. To make things more challenging, strong penetration power comes with much smaller cross-section for neutrons. Therefore, lengthy measurement time, usually tens of minutes to tens of hours even at facilities with most powerful neutron sources, is required to obtain high-quality data with the satisfactory signal-to-noise ratio.

The requirement of long measurement time not only limits the productivity of the neutron user facility but also has made real-time characterization experiments very challenging for neutron scattering techniques. For example, understanding dynamic response under external stimuli has been an active research field of nonequilibrium materials.[3,4] To understand the structural and dynamical changes in situ or operando, as in materials undergoing phase transition, external stimuli, or mechanical deformation, a snapshot of a material's structure and dynamics need to be taken periodically on a timescale relevant to the dynamic changes. While time-synchronized sample environment in combination with event-based processing of neutron data has enabled observation of fast dynamic changes even with neutrons,[5] irreversible phenomena can still be measured only with high enough flux. Therefore, minutes to tens of seconds of time resolution has been the best time resolution, which can provide good signals for studying irreversible process using neutron scatterings.[6–8] This is at least one or two orders of magnitude slower time resolution that x-ray scattering can achieve.[7–9] Considering the unique capabilities that neutrons have, enabling fast data collection using neutrons will bring new science opportunities in materials research. Hardware investment (constructing a bigger accelerator and/or using a brighter source) to solve these aforementioned problems is impractical, as the return on investment is not cost-effective. The spallation source has begun to reach its practically attainable flux limit, and there are still various challenges left for the new type of neutron production such as an inertial fusion method becomes realized.[10] In addition, neutron flux will still remain insufficient to measure weakly scattering samples or to capture faster dynamic processes requiring shorter counting time.

One way to speed up the measurement while keeping good counting statistics per detector pixel is to reduce the number of detector pixels and increase the individual pixel area. More neutrons per pixel will be collected if the area of the individual pixel is increased. Therefore, the same level of signal-to-noise ratio per individual pixel can be achieved much faster than high-resolution data collection which uses the smaller individual pixel area and more pixels. In short, the measurement speed is gained at the sacrifice of resolution. However, if high-resolution detector images can be recovered from the given low-resolution input, this will result in effective speed-up of the neutron experiments without compromising resolution. Super-resolution is an active research topic in digital image

processing and computer vision,[11] where mostly nature (electro-optical) images are studied. Here, we adopt the state-of-the-art super-resolution algorithm to neutron scattering data. The aim is to recover a high-resolution image from its low-resolution signal. Due to physical acquisition limitations in image formation, high-resolution images are, in general, harder (or require longer time) to capture. Thus, the super-resolution technique can be applied to improve the efficiency in the acquisition of high-resolution information from merely the observed low-resolution signals. Super-resolution is an ill-posed problem since a single pixel in a low-resolution image could map to multiple pixels in its high-resolution counterparts. A key assumption of many super-resolution techniques is that the high-frequency pattern is redundant and can be easily reconstructed from low-frequency components. Existing super-resolution methods can be organized into three categories: (i) edge-based methods, (ii) image statistical methods, and (iii) example patch-based methods.[11] Example patch-based methods have achieved good performance in traditional methods.[12–15] Sparse dictionary learning (or sparse coding) is widely used in these methods, which assumes that the image signal can be represented by a dictionary of representation atoms. This way, the redundant patterns of high-frequency signals can be represented by dictionary atoms, and the correspondence between low-resolution and high-resolution representations is learnt through the sparsity-based formulation.[12,13]

Recently, due to the booming popularity of deep learning and in artificial intelligence,[16] deep neural networks (DNNs)-based methods can achieve the excellent performance in many research fields including image analysis, healthcare, and natural language processing. Specific to our problem here, deep convolutional neural network (CNN)-based image super-resolution methods have shown promising results in enhancing low-resolution or noisy images by learning from sufficiently large training examples.[17,18] DNN models are known to be capable of learning superior features that can improve the reconstruction accuracy in super-resolution. Several DNNs-based super-resolution methods[17,19,20] with end-to-end learning have shown superior performance than the traditional sparse coding methods based on hand-crafted features. The basic idea of these methods is to learn a good feature representation in the top several layers of neural networks and map the low-level feature to high-resolution signal space. The whole process is trained end-to-end with little pre/postprocessing beyond the optimization. We have recognized a great potential of applying the deep learning image super-resolution approach to accelerate neutron scattering data collection, particularly small-angle neutron scattering (SANS) data to begin with, by taking advantage of large data sets available at EQ-SANS (SNS, Oak Ridge).

In this work, we apply the one of the well-known super-resolution CNNs[17] to predict high-resolution scattering images from the low-resolution scattering inputs. A super-resolution neural network is trained by using randomly selected SANS data sets under identical instrument configuration from EQ-SANS at SNS. The results show the proof of concept that the super-resolution method can potentially accelerate the experimental workflow by identifying important features at the early stage of measurement.

Methods

Data preparation

We prepare the SANS data collected from EQ-SANS at SNS to train a deep image super-resolution neural network. As of August 2018, EQ-SANS has collected more than 80,000 measurements including both transmission and scattering data at various configurations. Each instrument configuration, such as sample-to-detector distance, choices of beam slits, sample apertures, and wavelength bands, introduces unique resolution function and q-ranges, where the wavevector q is defined as $q = 4\pi\sin(\theta)/\lambda$ with scattering angle θ and wavelength λ. These are critical parameters that determine the broadening of scattering peaks and typically observed scattering patterns. For reasonable training, pairs of scattering images both at low-resolution and high-resolution are required. In order to isolate the effect of noise in the data, scattering images that have more than five million total neutron counts are preselected. Data sets are further filtered by the most widely used instrument configuration, which is 4 m sample-to-detector distance and a wavelength band with 2.5 Å as a minimum wavelength. As a result, total 5573 scattering data have been selected and reduced in two resolutions (120×120 and 30×30) following standard SANS data reduction procedure using MantidPlot described elsewhere.[21] At this stage, the time-of-flight data have been reduced to static two-dimensional (2D) data. During the process of the data, the material and science-specific data were all removed from the metadata. Resulting three-column data (intensity, q_x, q_y) have been converted into the 2D array, where the value of each element is the scattering intensity at the position of q_x and q_y. We filled the element with 0 if the value of that position is missing.

Preprocessing

The intensity of input data is of a large range ($0 <$ intensity $< \sim 51{,}000$), where most of the intensity value are greater than 10,000. Data points of low intensity (less than 100) are sparse. The unbalanced data value can cause backpropagation optimization hard to converge during the training of neural networks. It can also reduce the accuracy of network outputs. Therefore, we applied the log normalization method on data to rescale it to a smaller range.

$$x' = \ln(x + \varepsilon),$$

where ε is set to make the base positive, and we use $\varepsilon = 3$ in our experiment. After rescaling, the range of input is (0, 16). After super-resolution, the output of the neural network will be rescaled to its original range by an inverse operation to obtain a value in its original range.

Neural network model

In this work, we adopt the Efficient Sub-Pixel Convolutional Neural Network (ESPCN)[17] for our experiment due to its good performance and time-efficiency. The ESPCN takes a low-resolution (LR) image (signal) $\mathbf{I}^{\mathrm{LR}}$ with tensor size $H \times W \times C$ as input, where C is the color channel and try to estimate the high-resolution (HR) ground truth $\mathbf{I}^{\mathrm{HR}}$ with a specified up-scaling ratio r. We denote the output of the neural network as $\mathbf{I}^{\mathrm{SR}}$, which has the same tensor size with $\mathbf{I}^{\mathrm{HR}}$ as $rH \times rW \times C$. The architecture of ESPCN consists of two parts: the first $L-1$ convolutional layers are applied to $\mathbf{I}^{\mathrm{LR}}$ to learn the feature representation of input signal, then a sub-pixel convolution layer upscales the low-resolution feature maps to produce $\mathbf{I}^{\mathrm{SR}}$.

The first $L-1$ convolutional layers can be represented as follows:

$$f^1(\mathbf{I}^{\mathrm{LR}}; W_1, b_1) = \phi(W_1 \times \mathbf{I}^{\mathrm{LR}} + b_1),$$
$$f^l(\mathbf{I}^{\mathrm{LR}}; W_{1:l}, b_{1:l}) = \phi(W_l \times f^{l-1}(\mathbf{I}^{\mathrm{LR}}) + b_l),$$

where W_l, b_l, $l \in [1, L-1]$ are learnable network weights and bias for each convolutional layer. $\varphi(\cdot)$ is the nonlinear activation function. The Rectified Linear Unit (ReLU) used in the network as the activation function is

$$\mathrm{ReLU}(x) = \max(0, x).$$

After the first $L-1$ convolutional layers, $\mathbf{I}^{\mathrm{LR}}$ is represented by an $H \times W \times r^2C$ tensor. To generate the desired high-resolution image $\mathbf{I}^{\mathrm{SR}}$ from LR feature maps, a sub-pixel convolution layer is used of a deconvolutional layer as in Ref. [22]. Both proposed sub-pixel convolution layer and deconvolutional layer can map the same feature maps in LR space to HR space; however, the sub-pixel convolution layer contains more parameters in convolution filters, thus with more representation capability in up-sampling the input signal with the same computational speed. The last sub-pixel convolution layer is formulated as follows:

$$\mathbf{I}^{\mathrm{SR}} = f^L(\mathbf{I}^{\mathrm{LR}}) = \mathrm{PS}(W_L \times f^{L-1}(\mathbf{I}^{\mathrm{LR}}) + b_L),$$

where PS is a periodic shuffling operator that rearranges the elements of an $H \times W \times r^2C$ tensor to a tensor with a shape $rH \times rW \times C$, which is the estimated super-resolution image $\mathbf{I}^{\mathrm{SR}}$. Detailed implementation can be found in Refs. [17,23]. To train the parameters of the network, a pixel-wise mean squared error (MSE) loss is applied as the objective function to measure the reconstruction errors:

$$\ell(W_{1:L}, b_{1:L}) = \frac{1}{r^2HW} \sum_{i=1}^{rH} \sum_{j=1}^{rW} (\mathbf{I}^{\mathrm{HR}}_{i,j} - f^L_{i,j}(\mathbf{I}^{\mathrm{LR}}))^2.$$

Training settings

For the ESPCN, we followed the default setting of neural networks in Ref. [17] and set the upscale factor $\mathbf{r} = 3$. They take 70% of data samples for training and the remaining 30% samples for testing. The learning rate is set to 0.001. The training loss is converged after 2000 epochs. The ESPCN is implemented using PyTorch,[24] a popular scientific computing library. The training process takes roughly 3 h on an NVIDIA TITAN X GPU using 3800 training samples. The accuracy of the super-resolution results is discussed via (i) qualitative comparison of the 2D scattering images and (ii) estimation of χ^2 between the 1D scattering intensities of super-resolution results and corresponding ground truth data. In both trainings and testings, information of the samples are not used. Therefore, all training and test cases are chosen randomly regardless of what actual samples are.

Results

Figure 1(a) shows an example of super-resolution result in comparison with the baseline bicubic up-sampling applied to the raw SANS data. The input image is in the resolution of 30×30 pixels. High-resolution prediction is 120×120, which is 16 times more pixels. The scattering image shown here exhibits one of the commonly observed scattering characteristics of SANS data. The scattering intensity is strongest at the lowest q value and decays as the q increases. Both bicubic algorithm and the proposed deep learning super-resolution method, for simplicity denoted as AI method, successfully predict the decaying intensity as a function of q qualitatively well. However, note that the AI predicted image not only produced the scattering intensity profile but also produced one of the instrument features, a beamstop. In SANS experiments, the beamstop is often used to block the direct beam of neutrons. The beamstop absorbs neutrons; therefore, it appears as empty pixels. At EQ-SANS, 60-mm-diameter beamstop is used for 4 m sample-to-detector distance configuration. The detector of EQ-SANS has an intrinsic pixel size of 5.5 mm × 4.3 mm.[25] Therefore, the size of the beamstop is less than 10–15 pixels in width and height, respectively. However, the area of pixels shadowed by the beamstop is shown smaller in q-space due to the wide wavelength bands and the number of q-space bins. The pixel size of the low-resolution image is estimated to be around ~20 mm in real space. Therefore, the beamstop does not show up in the low-resolution q-space image, due to the scattering intensities contributed from different wavelengths [Fig. 1(a), low-resolution input]. Since there is no clear evidence of empty pixels representing a beamstop, bicubic algorithm fills the center pixels with predicted intensity. However, trained AI has identified the beamstop as one of the instrument features and predicted positions of the empty pixels in the high-resolution output [Fig. 1(a), AI] even when the beamstop is not visually identified in the low-resolution input. In Fig. 1(b), the 1D averaged scattering intensities from different sources are compared. Both results from the bicubic algorithm and the AI prediction overlap with the ground truth well for $q > 0.03$ Å^{-1}. It is mainly due to the continuous and monotonic nature of this type of scattering profile, where the bicubic algorithm can perform excellent. However, it should be pointed out that the AI predicted curve showed better

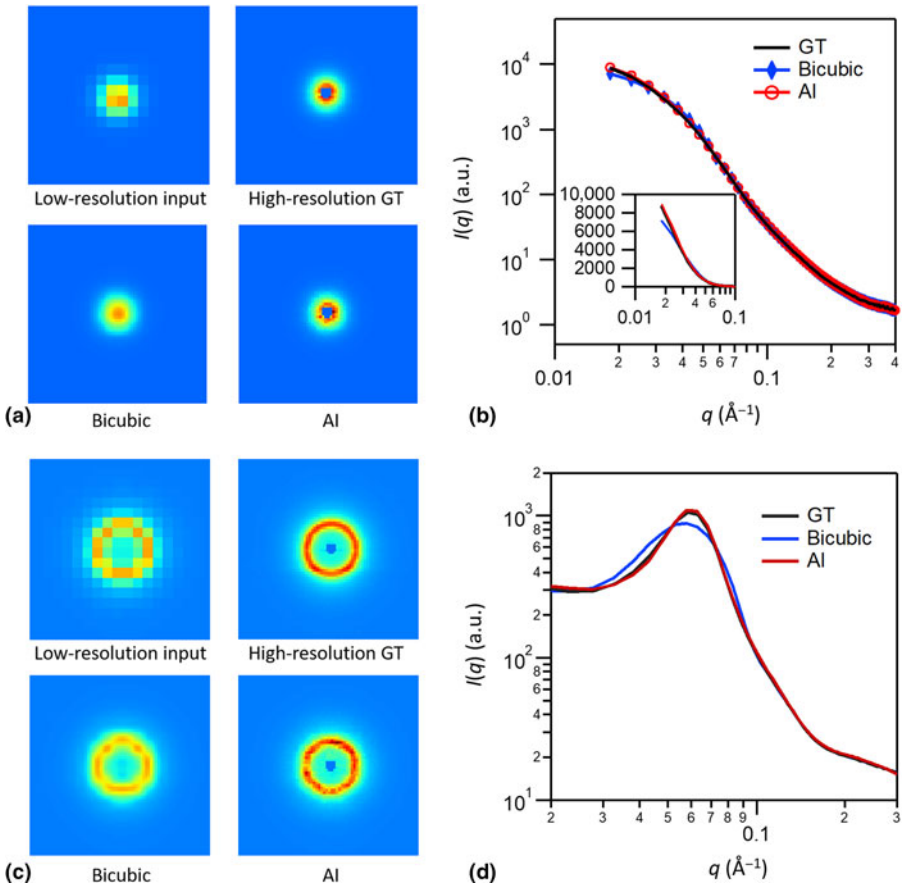

Figure 1. Example of super-resolution AI on SANS data showing monotonic decay of scattering intensity as a function of *q*. (a) 2D data showing low-resolution input, high-resolution ground truth (GT), high-resolution image predicted by the bicubic algorithm, and high-resolution image predicted by the AI model trained using EQ-SANS data. Images shown here are cropped around the centers of the full images to help visual comparison. (b) Circular averaged scattering profiles of the 2D data shown in (a). Bicubic and AI results are also shown with markers to help visual inspection of the differences. Inset is the scaled-up plot of the low-*q* range with the linear *y*-axis. (c) Example of 2D SANS data with anisotropic peak. (d) Circular averaged scattering profiles of the data shown in (c).

accuracy, especially at low-*q* ranges, while the bicubic algorithm produced more deviations from the ground truth than the AI model.

We next apply the AI super-resolution model on another commonly encountered scattering pattern of SANS and compare the result with that from the bicubic algorithm. The isotropic ring pattern is often observed from SANS measurements, indicating strong correlation at a certain length scale. For examples, interacting colloidal systems exhibit correlation peak whose width and sharpness can provide critical information about the distribution of particles and characteristics of interaction potentials. Randomly oriented liquid crystalline phase also produces scattering peaks, which will appear as rings in 2D scattering pattern. The position and width of the rings can be used to extract structural dimensions and degree of order.[26,27] Therefore, the super-resolution algorithm has to produce the correct position and width of such scattering features from the low-resolution input in order for the predicted scattering images to provide reliable information for further utilization. In Fig. 1(c), results from the bicubic algorithm and the AI model are compared. The AI super-resolution model has shown significantly better performance in recovering peak position and peak width compared to the bicubic algorithm. Bicubic algorithm resulted in a distorted ring shape in 2D with much broader peak width, which would give the incorrect physical interpretation. The difference in the peak shape can be clearly observed from the 1D averaged scattering curve in Fig. 1(d). The bicubic algorithm not only fails to predict the correct width of the peak but also predicts the peak position slightly off. In contrast, the AI model's prediction practically overlaps with the ground truth data.

In SANS, anisotropic 2D scattering patterns can be observed from samples that exhibit molecular level alignment and orientation. Soft materials under shear or stretching are well-known examples that show such alignment, resulting in anisotropic scattering patterns.[28–30] In principle, microstructures of deformed soft materials can be studied from the anisotropic scattering patterns, which can elucidate the relation between

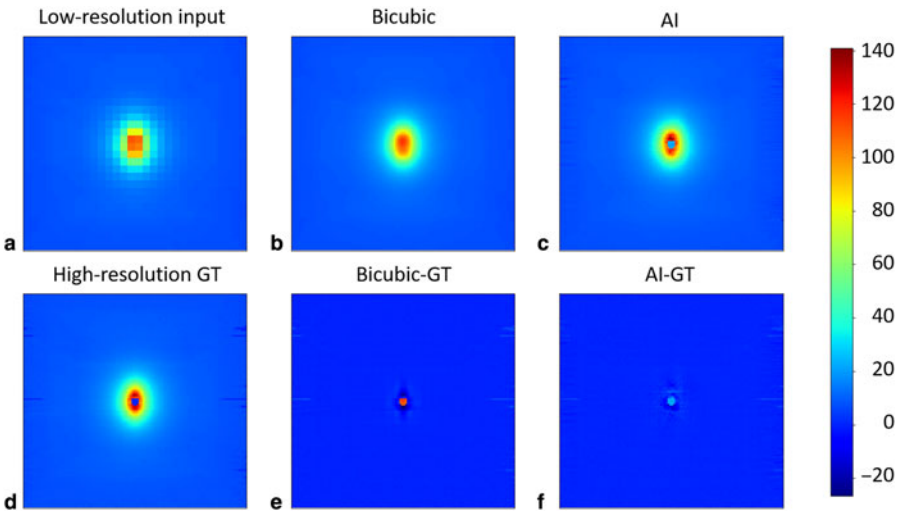

Figure 2. Example of the super-resolution process on a 2D anisotropic scattering image. (a) Anisotropic 2D scattering image was used as an input to 2D data showing the low-resolution input for super-resolution algorithms. Results with an enhanced resolution by (b) the bicubic algorithm and (c) the AI model are shown. (d) High-resolution ground truth image. (e) and (f) Differences between the images obtained by the super-resolution algorithms and the ground truth.

the structural deformation and resulting physical properties. Recent theoretical and experimental studies[31,32] have also proved the importance of quantitative analysis on 2D scattering data for the fundamental understanding of rheological behavior. Our AI model has shown success in predicting the high-resolution scattering pattern from the low-resolution anisotropic scattering data as well. Figure 2 shows a typical anisotropic pattern of SANS measured at low-resolution and its high-resolution counterpart along with predictions by the bicubic algorithm and the AI model. From the 2D pattern, both high-resolution images reconstructed by the AI and bicubic algorithm show similar anisotropy found in the ground truth image. This again shows that the bicubic algorithm works reasonably well when the scattering profile has slow and monotonic q dependency without sharp transitions. The anisotropy represented by the integrated intensity from $0.03\ \text{Å}^{-1} < q < 0.1\ \text{Å}^{-1}$ along the annulus also indicate the level of anisotropy is well reproduced by both algorithms [Fig. 3(a)]. One-dimensional scattering intensities from the predicted 2D patterns are also compared by taking ±10° sectional average along the horizontal and vertical direction. In anisotropic scattering data analysis, scattering intensity profiles of specific orientation carry important information about the anisotropic structure of the sample. While both algorithms predicted the horizontal profiles with the reasonably good agreement [Fig. 3(b)], AI prediction showed slightly better performance in reconstructing scattering intensity along the vertical direction [Fig. 3(c)].

In general, the AI model seems to be more accurate in predicting scattering images with sharp transitions. Since the bicubic algorithm relies on the smoothing and interpolation of data from one pixel to another, any lost information within a pixel

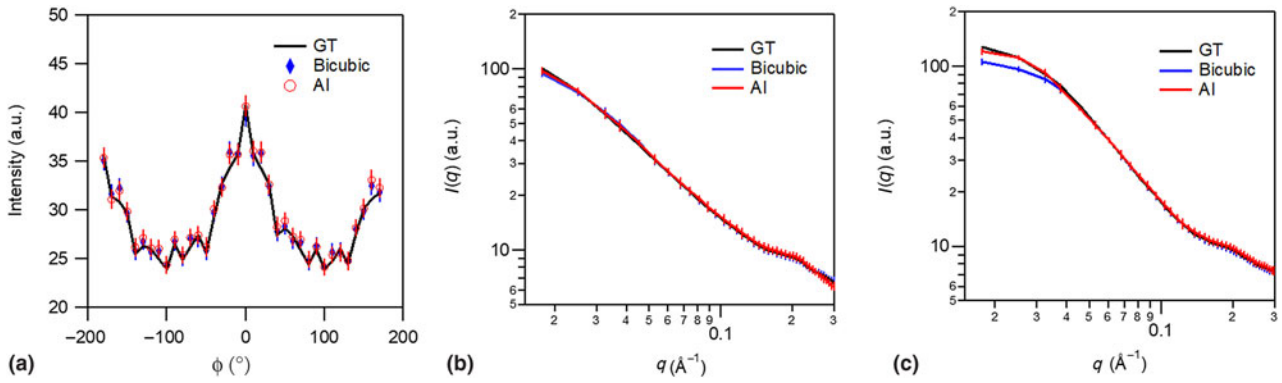

Figure 3. (a) Annulus plot of integral intensities showing the anisotropic character of the 2D data. (b) Sectional average along the horizontal direction of scattering patterns from Fig. 2. (c) Sectional average along the vertical direction of scattering patterns from Fig. 2.

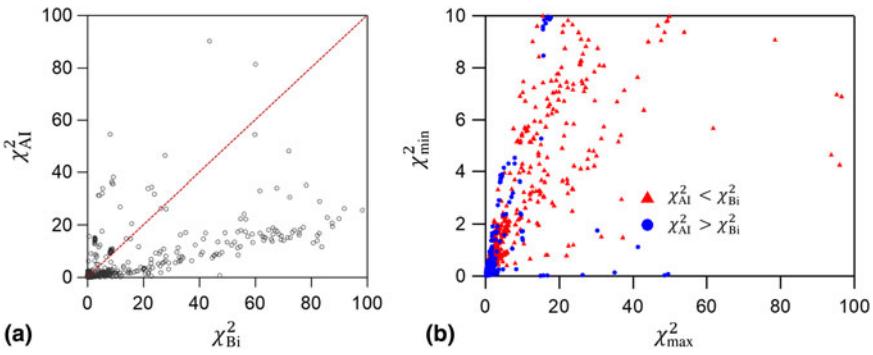

Figure 4. (a) Distribution of χ^2 from the AI and bicubic super-resolution algorithm. Dashed line indicates equal performance. (b) Distribution of χ^2 values for cases with $\chi^2_{min} < 10$. Red triangles indicate cases where the AI performed better than the bicubic algorithm based on χ^2 values. Blue circles represent cases where the bicubic algorithm resulted in smaller χ^2 values.

cannot be recovered to a higher-resolution image. On the other hand, the AI model is trained and equipped with a unique database that can connect the low-resolution pixel-to-pixel correlation information to a detailed high-resolution information. This enables for the AI model to grasp the attainable sharpness in the high-resolution training images, which may be described as an instrument resolution kernel.

In order to provide overall performance comparison between the AI model and the bicubic algorithm, differences between 1D averaged $I_{AI}(q)$ and $I_{GT}(q)$ have been estimated for all 1662 test cases using $\chi^2 = \sum (I_{AI\,or\,Bi}(q) - I_{GT}(q))^2/N$, where N is the number of q values used in the summation. The q range ($0.02\ \text{Å}^{-1} < q < 0.3\ \text{Å}^{-1}$) used in this calculation was chosen to exclude the shadowed pixels by the beamstop because the inclusion of these pixels will give a huge penalty for the bicubic algorithm, which do not produce the null pixels intrinsically. The results are summarized in Fig. 4(a) along with a dashed line indicating equal performance between the AI model and the bicubic model. It is clear that χ^2 values from the bicubic model (χ^2_{Bi}) are overall higher than the ones from the AI model (χ^2_{AI}), suggesting that the AI model performs better than the bicubic algorithm. A closer look at the results is found in Fig. 4(b) where only the cases (1420 cases out of 1662) with at least one of the χ^2 values being less than 10. A smaller value of the two χ^2 values is denoted as χ^2_{min}, and the other is denoted as χ^2_{max}. This subset describes that quantitatively good prediction for the high-resolution scattering images has been achieved by one of the two algorithms. Red triangles indicate test cases where the AI model's prediction was quantitatively better than the bicubic algorithm. And the blue circle represents test cases where the bicubic algorithm had smaller χ^2. Interestingly, the distribution between red and blue data points can tell us about the effectiveness of the AI model. The fact that blue data points are well concentrated in the $\chi^2_{max} < 10$ region shows that both the AI and bicubic models predicted the high-resolution images reasonably well and the difference between the predictions was small. However, when the AI was more successful than the bicubic algorithm [red triangles in Fig. 4(b)], the χ^2_{max} values extend relatively large up to ~100. In other words, AI's prediction made much more significant improvements over the bicubic predictions.

Discussion

We have demonstrated a proof of concept approach to allow SANS data collection with low-spatial resolution and then subsequently recovering the high-resolution data by using a deep learning-based super-resolution method. By utilizing randomly selected SANS data from an identical instrument configuration, a super-resolution DNN model has been trained. Results show that the super-resolution model trained in this way can successfully reconstruct high-resolution scattering images from the low-resolution data. Especially, our examples have succeeded in restoring features such as scattering peaks with narrow width better than the traditional bicubic algorithm. The success may be attributed to the fact that the DNN-based super-resolution model was able to capture instrument-specific characteristics such as the presence of the beamstop and instrument resolution, which determines the broadening of scattering peaks, during the training process. Being able to use low-resolution detector images is equivalent to reducing measurement time. In this study, we have shown that the high-resolution scattering data can be recovered from the low-resolution data with 16 times bigger pixel areas. Therefore, the same level of counting statistics can be achieved at 16 times faster rate. This allows users to make critical decisions on whether to continue on-going data collection or move to next samples at a much earlier stage of data collection. Such fast-decision making can accelerate the overall experimental workflow of SANS measurements and enables more efficient use of beamtime. Considering that a huge amount of costs and efforts are typically required to improve neutron flux or the performance of an instrument by 10 times, the approach proposed in this research may provide new opportunities in neutron scattering sciences. If successfully integrated with existing beamlines after further studies on the choices of neural network models

and training data sets, this method will not only accelerate the scientific process as it can help scientists' early decision making but also enable time-resolved scattering experiments at timescales which have not been possible before.

Acknowledgment

The Research at Oak Ridge National Laboratory's Spallation Neutron Source was sponsored by the Scientific User Facilities Division, Office of Basic Energy Sciences, U.S. Department of Energy.

References

1. P. Lindner and T. Zemb (eds): *Neutrons, X-Rays and Light: Scattering Methods Applied to Soft Condensed Matter* (North-Holland, The Netherlands, 2002).
2. D. Richter, M. Monkenbusch, A. Arbe, and J. Colmenero: Neutron Spin Echo in Polymer Systems, Vol. 174 (Springer, Berlin, Heidelberg, 2005), p. 1.
3. T. Narayanan, H. Wacklin, O. Konovalov, and R. Lund: Recent applications of synchrotron radiation and neutrons in the study of soft matter. *Crystallogr. Rev.* **23**, 160 (2017).
4. C.J. Milne, T.J. Penfold, and M. Chergui: Recent experimental and theoretical developments in time-resolved X-ray spectroscopies. *Coord. Chem. Rev.* **277–278**, 44 (2014).
5. G.E. Granroth, K. An, H.L. Smith, P. Whitfield, J.C. Neuefeind, J. Lee, W. Zhou, V.N. Sedov, P.F. Peterson, A. Parizzi, H. Skorpenske, S.M. Hartman, A. Huq, and D.L. Abernathy: Event-based processing of neutron scattering data at the Spallation Neutron Source. *J. Appl. Crystallogr.* **51**, 616 (2018).
6. R. Lund, L. Willner, D. Richter, H. Iatrou, N. Hadjichristidis, P. Lindner, and IUCr: Unraveling the equilibrium chain exchange kinetics of polymeric micelles using small-angle neutron scattering—architectural and topological effects. *J. Appl. Crystallogr.* **40**, s327 (2007).
7. L.K. Bruetzel, P.U. Walker, T. Gerling, H. Dietz, and J. Lipfert: Time-resolved small-angle X-ray scattering reveals millisecond transitions of a DNA origami switch. *Nano Lett.* **18**, 2672 (2018).
8. A. Sauter, F. Roosen-Runge, F. Zhang, G. Lotze, R.M.J. Jacobs, and F. Schreiber: Real-time observation of nonclassical protein crystallization kinetics. *J. Am. Chem. Soc.* **137**, 1485 (2015).
9. K. Vegso, P. Siffalovic, M. Jergel, P. Nadazdy, V. Nadazdy, and E. Majkova: Kinetics of polymer–fullerene phase separation during solvent annealing studied by table-top X-ray scattering. *ACS Appl. Mater. Interfaces* **9**, 8241 (2017).
10. A. Taylor, M. Dunne, S. Bennington, S. Ansell, I. Gardner, P. Norreys, T. Broome, D. Findlay, and R. Nelmes: A route to the brightest possible neutron source? *Science* **315**, 1092 (2007).
11. Z. Wang, J. Chen, and S.C.H. Hoi: *Deep Learning for Image Super-Resolution: A Survey* (2019). arXiv:1902.06068 [Cs.CV].
12. J. Yang: Image super-resolution via sparse representation. *IEEE Trans. Image Process.* **19**, 2861 (2010).
13. W. Dong, L. Zhang, G. Shi, and X. Wu: Image deblurring and super-resolution by adaptive sparse domain selection and adaptive regularization. *IEEE Trans. Image Process.* **20**, 1838 (2011).
14. K.I. Kim and Y. Kwon: Single-image super-resolution using sparse regression and natural image prior. *IEEE Trans. Pattern Anal. Mach. Intell.* **32**, 1127 (2010).
15. J. Yang, Z. Lin, and S. Cohen: Fast image super-resolution based on in-place example regression. *Proceedings of the IEEE Conference on Computer Vision and Pattern Recognition,* 1059 (2013).
16. Y. LeCun, Y. Bengio, and G. Hinton: Deep learning. *Nature* **521**, 436 (2015).
17. W. Shi, J. Caballero, F. Huszar, J. Totz, A.P. Aitken, R. Bishop, D. Rueckert, and Z. Wang: Real-time single image and video super-resolution using an efficient sub-pixel convolutional neural network. *IEEE Conference on Computer Vision and Pattern Recognition* 1874 (2016).
18. A. Krizhevsky, I. Sutskever, and G.E. Hinton: ImageNet classification with deep convolutional neural networks. *Advances in Neural Information Processing Systems* 1097 (2012).
19. Y. Chen and T. Pock: Trainable nonlinear reaction diffusion: a flexible framework for fast and effective image restoration. *IEEE Trans. Pattern Anal. Mach. Intell.* **39**, 1256 (2017).
20. C. Dong, C.C. Loy, K. He, and X. Tang: Image super-resolution using deep convolutional networks. *IEEE Trans. Pattern Anal. Mach. Intell.* **38**, 295 (2016).
21. W.T. Heller, M. Cuneo, L. Debeer-Schmitt, C. Do, L. He, L. Heroux, K. Littrell, S.V. Pingali, S. Qian, C. Stanley, V.S. Urban, B. Wu, W. Bras, and IUCr: The suite of small-angle neutron scattering instruments at Oak Ridge National Laboratory. *J. Appl. Crystallogr.* **51**, 242 (2018).
22. E. Shelhamer, J. Long, and T. Darrell: Fully convolutional networks for semantic segmentation. *IEEE Trans. Pattern Anal. Mach. Intell.* **39**, 640 (2017).
23. W. Shi, J. Caballero, L. Theis, F. Huszar, A. Aitken, C. Ledig, and Z. Wang: *Is the Deconvolution Layer the Same as a Convolutional Layer?* (2016). arXiv:1609.07009 [Cs.CV].
24. A. Paszke, S. Gross, S. Chintala, G. Chanan, E. Yang, Z. DeVito, Z. Lin, A. Desmaison, L. Antiga, and A. Lerer: Automatic differentiation in PyTorch. In *NIPS-W*, Long Beach, USA (2017).
25. J.K. Zhao, C.Y. Gao, and D. Liu: The extended Q-range small-angle neutron scattering diffractometer at the SNS. *J. Appl. Cryst.* **43**, 1068 (2010).
26. F. Castro-Roman, L. Porcar, G. Porte, and C. Ligoure: Quantitative analysis of lyotropic lamellar phases SANS patterns in powder oriented samples. *Eur. Phys. J. E* **18**, 259 (2005).
27. C. Doe, H.-S. Jang, S.R. Kline, and S.-M. Choi: Subdomain structures of lamellar and reverse hexagonal pluronic ternary systems investigated by small-angle neutron scattering. *Macromolecules* **42**, 2645 (2009).
28. Z. Wang, T. Iwashita, L. Porcar, Y. Wang, Y. Liu, L.E. Sanchez-Diaz, B. Wu, T. Egami, and W.-R. Chen: *Dynamically Correlated Region in Sheared Colloidal Glasses Revealed by Neutron Scattering* (2017). arXiv:1709.07507.
29. C.R. López-Barrón, Y. Zeng, J.J. Schaefer, A.P.R. Eberle, T.P. Lodge, and F.S. Bates: Molecular alignment in polyethylene during cold drawing using in-situ SANS and Raman spectroscopy. *Macromolecules* **50**, 3627 (2017).
30. K. Mortensen: Structural studies of aqueous solutions of PEO—PPO—PEO triblock copolymers, their micellar aggregates and mesophases; a small-angle neutron scattering study. *J. Phys. Condens. Matter* **8**, A103 (1996).
31. Z. Wang, C.N. Lam, W.-R. Chen, W. Wang, J. Liu, Y. Liu, L. Porcar, C.B. Stanley, Z. Zhao, K. Hong, and Y. Wang: Fingerprinting molecular relaxation in deformed polymers. *Phys. Rev. X* **7**, 031003 (2017).
32. G.-R. Huang, Y. Wang, B. Wu, Z. Wang, C. Do, G.S. Smith, W. Bras, L. Porcar, P. Falus, and W.-R. Chen: Reconstruction of three-dimensional anisotropic structure from small-angle scattering experiments. *Phys. Rev. E* **96**, 022612 (2017).